PAPER

Quality Features for Holistic Evaluation and Quality Control of Micro Face Gears

Ali Bilen[1,*], Lennart Ernst[1], Edouard Gindin[2], Jannick Schubert[1], Magnus Rauwolf[1], Erik Leon Rauschenberg[1], Sebastian Michael Schnaith[1], Theresa Edelmann[1], Martin Benfer[1,*], Gisela Lanza[1,3]

[1]wbk Institute of Production Science, Karlsruhe Institute of Technology (KIT), Karlsruhe, Germany
[2]FRENCO GmbH, Altdorf, Germany
[3]GAMI – Global Advanced Manufacturing Institute, Moon Bay Road 10
[*]Corresponding author

E-mail: ali.bilen@kit.edu

Keywords: Face gears, Micro gearing, Geometric inspection, Gear metrology, Holistic quality evaluation, Quality control

Abstract

Micro face gears exhibit complex non-involute flank geometry and lack standardized inspection concepts. In contrast to cylindrical gears, where VDI 2612 provides interpretable profile, flank and pitch characteristics, face gear quality assessment remains fragmented and qualitative. This work presents a feature-based evaluation strategy for micro face gears that transfers cylindrical inspection logic and extends it with dedicated diagnostic features for axial infeed and tangential misalignment. Optical scan data are converted into profile-, flank- and pitch-inspired descriptors within the functional engagement region, establishing a geometric interface between metrology and process parameters in micro-scale hobbing. The strategy is validated on 225 experimentally manufactured face gears with intentionally varied axial infeed, tangential shift and spindle wobble. The results show that these deviation modes can be separated based on their geometric responses, indicating diagnostic capability suitable for virtual metrology and process correction.

1 Introduction

Face gears, which represent the transition from conical external to internal gearing and can be defined as a special case of bevel gears with a pitch cone angle of 90° [22], play an increasingly important role in compact and high-performance drive systems [18]. Their geometric configuration offers advantages such as high contact ratios, reduced sensitivity to alignment errors, and favorable load distribution, which is why they appear in aerospace, robotics, automotive applications and, in particular, in medical drive units and dental handpieces [21]. However, this functional robustness is achieved at the cost of a complex three-dimensional flank geometry [28] that significantly increases the demands on manufacturing and metrology.

A central difficulty in the inspection of face gears arises from their inherently three-dimensional flank geometry [7, 22, 11]. In contrast to cylindrical gears, the pressure angle varies continuously along the tooth axis [22], and the profile shape deviates fundamentally from an involute. As a consequence, classical line-based evaluation strategies are no longer directly applicable, and the assessment task becomes substantially more complex. What is required is a set of dedicated geometric features that not only quantify axial and lateral variations, but also reveal how characteristic deviations relate to adjustable manufacturing parameters and process-induced error mechanisms. This necessitates a formal logic that systematically transfers established evaluation concepts from cylindrical gearing to the three-dimensional geometry of face gears and renders them operational for diagnostic and corrective purposes.

These difficulties are amplified in the micro range. Below approximately $m < 0.2\,\text{mm}$, tactile metrology reaches physical limits due to stylus size, probing forces and restricted accessibility of functional surfaces [23, 10]. Consequently, micro face gears are predominantly captured using optical coordinate metrology. In contrast to tactile probing, which generates structured measurement data along predefined trajectories, optical systems produce unstructured data formats such as point clouds or STL meshes [6]. These data sets contain irregular point densities, noise, reflection artefacts, missing areas and undefined regions at steep flanks [10]. They cannot be evaluated without prior processing; before geometric inspection is possible, they must be aligned to a reference coordinate system, cleaned, segmented, and reduced to reproducible evaluation paths [19]. In other words, the metrological workload shifts from the measurement system to the evaluation strategy. The challenge is no longer only the correctness of the captured surface, but the transformation of raw optical scan data into meaningful input for gear-specific interpretation.

From an industrial perspective, this is particularly relevant as modern manufacturing increasingly targets closed-loop control concepts in which measured deviations are not merely documented but actively translated into corrective machine settings [14]. Current inspection practices for face gears, however, remain fragmented. This obstructs the identification of causal deviation mechanisms and prevents reliable derivation of process corrections.

The objective of this work is therefore to provide a holistic evaluation approach for micro face gears based on optical measurement data, capable of transforming unstructured scans into reproducible and interpretable parameters. By linking profile-, flank-, and pitch-related deviation patterns to typical manufacturing error mechanisms - such as axial shift, angular misalignment or tool offset - the method establishes a basis for diagnostic interpretation and forms the conceptual foundation for future closed-loop process control.

Contributions
The contributions of this work are threefold:

1. **Feature-based inspection logic for face gears.** Classical VDI 2612 profile-, flank- and pitch-related descriptors are systematically transferred to face gear geometry and extended to accommodate non-involute flank characteristics. This establishes an interpretable, metric-based inspection logic for micro face gears.

2. **Diagnostic features for tool parameter identification.** Two dedicated diagnostic features are introduced: the tooth thickness deviation for axial infeed estimation and the eccentricity indicator for detecting tangential misalignment. Together, these features enable a geometric interface between metrology and machine parameter space.

3. **Experimental validation under micro-scale metrology conditions.** The diagnostic capability of the feature set is validated on 225 experimentally manufactured face gears with intentionally introduced process deviations (axial infeed, tangential shift, spindle wobble). The experiments confirm separability of deviation mechanisms under realistic optical measurement uncertainty.

In combination, these contributions demonstrate that face gear geometry provides sufficient geometric observability to support diagnostic feedback and process correction in micro-scale hobbing.

2 Fundamentals

2.1 Geometry and Characteristics of Face Gears

Face gears represent a special class within bevel gearing and can be described as **non-involute bevel gears** with a pitch cone angle of $\delta = 90°$ meshing with a cylindrical spur pinion [22, p. 317]. Due to their non-involute geometry, established cylindrical-gear evaluation methods (DIN/VDI profile, flank, pitch deviation) **cannot be transferred directly**. Reference profiles, tolerance concepts, and standardized inspection logic therefore remain undefined for this gear type.

A defining characteristic is the *radius-dependent pressure angle* α, which varies continuously along the usable face width [12]. In contrast to cylindrical gears with constant pressure angle, the face gear flank must align with the radial direction to mesh with a spur pinion. As a consequence, the pressure angle decreases from the outer to the inner diameter.

The pressure-angle variation can be quantified by [22, 12] as

$$d_2 = \frac{m_n Z_2 \cos\alpha_n}{\cos\alpha_2}, \tag{1}$$

linking the macrogeometry to the local pressure angle α_2 at diameter d_2, where m_n denotes the normal module of the generating spur gear, Z_2 the number of face gear teeth, and α_n the nominal pressure angle of the spur pinion.

This radius dependency imposes geometric limits: at small radii, decreasing pressure angles lead to steep flanks and shortened involute segments (risk of undercutting), while large radii are limited by pointing effects.

These characteristics explain why face gears require dedicated evaluation features and metrological strategies rather than a direct application of spur-gear standards. The radius dependency, together with geometric boundary conditions, governs usable face width and load distribution.

Geometrical Properties and Deviation Directions Face gears are manufactured by a generative hobbing process in which the cutting tool emulates the mating spur pinion. The geometry emerges as the envelope of successive tool profiles. This generative principle, together with the resulting geometric characteristics relevant for metrological evaluation, is illustrated in Fig. 1.

Geometric deviations on face gears are typically analyzed along three principal directions: *profile*, *flank line*, and *pitch* [13]. While originating from cylindrical gear metrology, their interpretation in face gears is influenced by the radius-dependent geometry and the generative process.

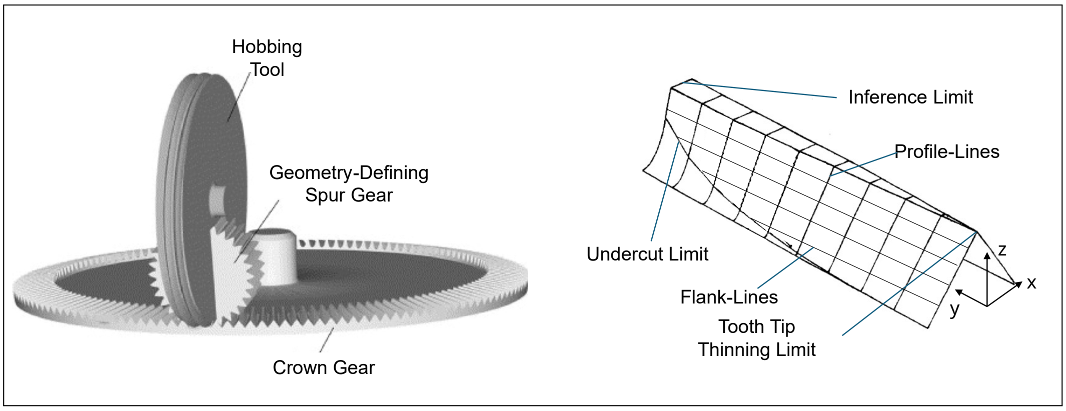

Figure 1: Generative manufacturing principle and resulting geometry of face gears. Left: hobbing process where the cutting tool emulates the mating spur pinion [18]. Right: resulting geometry with profile and flank line directions relevant for deviation analysis [17].

The *tooth profile* describes the flank in a normal section through the tooth height (xz-plane). Profile deviations influence load distribution, contact and efficiency [22]. In face gears, the attainable profile is restricted by pointing, interference, and undercut limits [22, 18]. The *flank line* represents the geometry along the face width (xy-plane). Due to the radius-dependent geometry, flank deviations cannot be evaluated independently of radial position. The *tooth pitch* describes the circumferential spacing of successive tooth flanks.

2.2 Specific Characteristics of Micro Gearing

Micro gears, as defined in VDI 2731, are characterized by small modules m, often $m < 200\,\mu$m, and fine structural detail [25]. In this range, tolerances cannot be linearly scaled from macro-gearing; extrapolated values lose technical meaning [25]. Additionally, manufacturing deviations and measurement uncertainty increasingly overlap. For $m < 0.2$ mm, tactile coordinate metrology approaches physical limits due to stylus size and probing forces [23]. This motivates the use of optical systems for fast areal acquisition, despite challenges with reflectivity and steep surface regions [10].

3 State of the Art

3.1 Evaluation of Gear Characteristics According to VDI 2612 and DIN ISO 1328

Precise metrology is essential for the quality assurance of gears, as geometric deviations directly affect efficiency, wear, and service life [23, p. 292]. While established standards such as DIN ISO 1328-1 and VDI/VDE 2612 exist for conventional cylindrical spur gears, no standardized framework is available for micro face gears. To nevertheless enable a systematic quality assessment, the established evaluation strategies are first introduced and subsequently transferred to the specific characteristics of face gears.

In industrial practice, the geometric evaluation of gears is commonly based on a decomposition into the four main deviation types *profile-line*, *flank-line*, and *pitch*, as well as runout errors, which are not considered further in this work (visualized in Fig. 2). These deviation components are obtained from a nominal–actual comparison between the measured geometry and the ideal involute reference geometry [23].

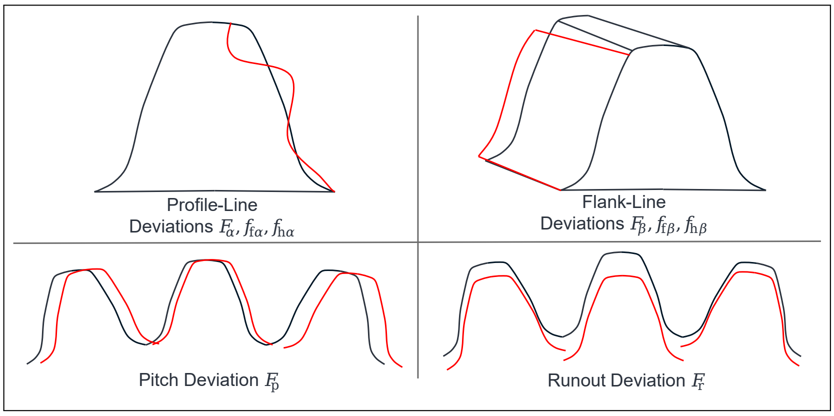

Figure 2: Typical deviations in cylindrical gear teeth (visualizations based on [8])

3.1.1 Profile and Helix Deviations According to VDI/VDE 2612 Blatt 1 [26], profile and helix form errors are systematically subdivided into a total deviation F, a slope-related component f_H, and a form-related component f_f.

Profile deviations from the nominal involute are determined along the involute within the active contact region. For this purpose, the guideline defines a specific evaluation range as well as a reduced regression range L_α for unmodified profiles. The total profile deviation F_α represents the maximum deviation within the active region L_{AE}, where the nominal involute is fitted such that it encloses the extreme values. The profile slope deviation $f_{H\alpha}$ is obtained by linear regression within the range L_α and corresponds to the distance between the intersections of the extended regression line (up to the addendum circle) and the nominal profile. After subtracting this slope component, the remaining pure profile form deviation $f_{f\alpha}$ is evaluated separately for the root, central, and tip regions.

Analogously, helix deviations are evaluated along the face width b. A regression range L_β, reduced by marginal zones, forms the basis of the evaluation. The total helix deviation F_β is determined using a double-line method that defines the maximum distance between the inner (material side) and outer (non-material side) nominal flanks. The helix slope deviation $f_{H\beta}$ describes the inclination of the regression line and indicates errors in the helix angle. After subtracting this component, the remaining helix form deviation $f_{f\beta}$ represents the local waviness of the tooth flank.

3.1.2 Pitch Deviations The assessment of uniform tooth spacing is conducted in accordance with DIN ISO 1328-1. The single pitch deviation f_p is defined as the maximum absolute value of the differences between actual and theoretical pitch (f_{p_i}) over all teeth and describes local positional errors of individual flanks.

For larger circumferential ranges, the total pitch deviation F_p is considered. It is obtained from the difference between the maximum and minimum values of the cumulative deviations (F_{p_i}) and is indicative of long-wavelength, systematic deviations in the manufacturing process.

3.1.3 Transferability to Micro Face Gears The direct application of the VDI 2612 evaluation scheme to micro face gears is only possible to a limited extent due to the complex, non-purely involute geometry and the lack of orthogonality between profile and helix directions. In addition, the very small module sizes significantly limit the applicability of classical tactile probing systems [23, p. 292].

Nevertheless, an adaptation of this feature structure is required in order to enable a three-dimensional error decomposition. Such an equivalent model allows measurement deviations to be systematically traced back to process parameters and forms the basis for a closed-loop quality control system in micro manufacturing [23, p. 650].

3.2 Quality Assessment of Face Gears

A review of the current literature reveals that no standardized, holistic evaluation methodology exists for face gears that is comparable to established standards for cylindrical gears. As a consequence, quality assessment approaches are fragmented across the analyzed studies.

This fragmentation contradicts the nature of face gears as complex three-dimensional objects and could be avoided by a clear structuring of error categories.

In general, gear errors can be classified into two major groups: form errors and positional errors. Form errors refer to deviations that alter the object geometry itself, such as surface deviations or displacements of individual teeth. Positional errors, also referred to as location errors, affect the positioning of the object as a whole or its interaction with other objects, such as mating gears or fixturing systems.

Due to their fundamentally different nature, these error groups require dedicated measurement strategies for reliable detection.

With respect to geometric measurement systems, tactile coordinate metrology remains the dominant approach. Lu et al. [20, p. 1] present an optical 3D scanning approach to increase the efficiency of point cloud acquisition but report accuracy limitations in boundary regions. Specific considerations for micro gears are not addressed; instead, the applications mainly focus on aerospace and automotive components [21, p. 1].

The evaluation strategies reveal a clear dichotomy: (1) either isolated individual parameters are determined, or (2) a global surface-based analysis is performed without reference to classical gear characteristics.

For instance, Lin et al. [15, p. 95] and Tao et al. [24, p. 15] focus on the computation of pitch deviations. In contrast, Lu et al. [21, p. 2] and Wang et al. [27, p. 18] analyze normal deviations of complete tooth surfaces. However, a methodological assignment of these global deviations to specific profile or helix slope errors-as required for process-integrated control loops-is not provided.

Bilen et al. [3] propose a unified quality evaluation for cylindrical and face gears by transforming the measured face gear geometry into an equivalent cylindrical gear geometry. This enables the application of established cylindrical gear characteristics and existing simulation tools, representing a significant step toward standardizing micro face gear inspection. The flank contact conditions of both gear types provide a solid foundation for this approach, although the mathematical formulation of the transformation model still involves open research questions.

Across the presented measurement strategies, a clear trend emerges: the determination of positional and location errors predominantly relies on holistic three-dimensional analyses. A central task within this category is the alignment of the 3D gear measurement, during which specific features such as eccentricity, wobble, or asymmetry are extracted.

However, the evaluation of face gear contact characteristics requires classical gear parameters according to VDI/VDE 2612. Their determination is only possible if a purely holistic 3D approach is abandoned in favor of analyzing selected two-dimensional sections of the face gear. These two tendencies are not mutually exclusive, enabling a combined strategy: 2D sections used to extract VDI/VDE 2612 gear characteristics can be aggregated into data packages that serve as a substitute for a full 3D representation, from which positional and location errors can subsequently be derived. measurement process.

4 Approach

This work presents a holistic evaluation strategy for face gears that enables closed-loop quality control in hobbing. The method derives actionable parameters directly from optical measurement data, allowing process adjustments rather than purely retrospective inspection. The approach follows four main stages explained in Sections 4.1 through 4.4: (i) definition of a consistent coordinate system as the geometric reference, (ii) preprocessing and registration of the 3D scans, (iii) point-wise computation of nominal-to-actual distances, and (iv) evaluation of these deviations in analogy to VDI 2612 to obtain profile, flank line, and pitch parameters adapted to face gear geometry. In Section 4.5, a dedicated feature for tangential positioning errors is introduced. Section 4.6 formulates hypotheses on how the investigated manufacturing deviations affect the derived parameters, establishing the basis for the exemplary quality control application in Chapter 5.

4.1 Reference Coordinate System and Symbols

The geometric evaluation is performed in a gear-fixed Cartesian coordinate system (visualized in Fig. 3. The y-axis coincides with the tooth axis of the face gear, while the x-axis is oriented perpendicular to the tooth axis within the plane of the gear. Consequently, the x–y plane represents the planar reference surface of the face gear. The z-axis is oriented normal to this plane and corresponds to the axial direction of the gear. This coordinate system serves as the common reference frame for all geometric evaluations and feature definitions used in this work. For clarity and consistency, all symbols and variables introduced in the following sections are summarized in a dedicated list of symbols.

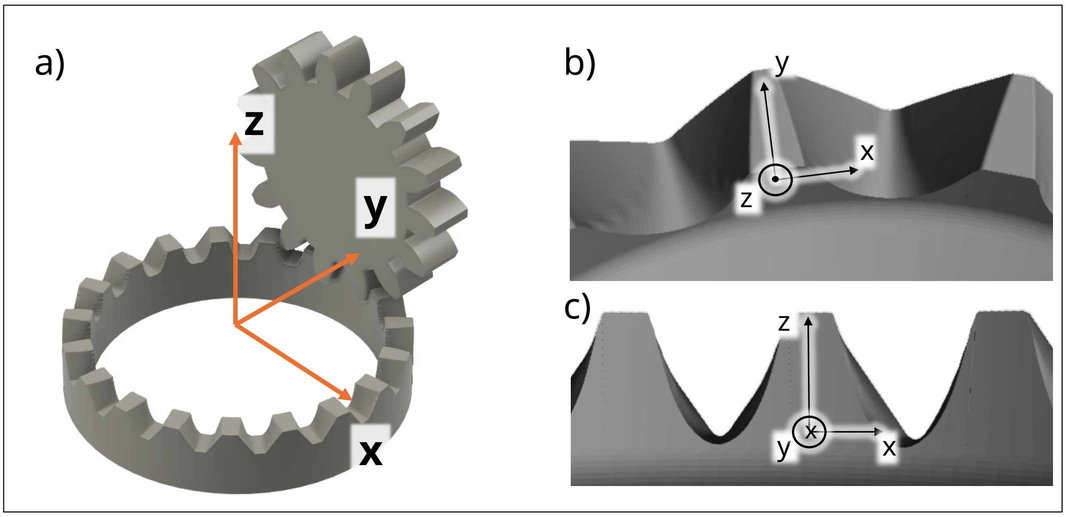

Figure 3: Coordinate System [7], a) based on [4]

List of Symbols

Symbol	Description
a	Slope of the linear regression line (profile or flank line)
b	Intercept of the linear regression line
d_i	Point-wise distance between nominal and actual geometry
d_{norm}	Signed normal distance between nominal and actual geometry
$f_{f\alpha},\ f_{f\beta}$	Form deviation of profile / flank (residual after slope removal)
$f_{H\alpha},\ f_{H\beta}$	Slope / angle deviation of the profile or flank line
$F_\alpha,\ F_\beta$	Total profile / flank deviation (peak-to-valley)
F_p	Total pitch deviation
f_p	Single pitch deviation
m_n	Normal module
n	Number of axial slicing planes
N	Number of evaluated points
r_e	Eccentric radius; diagnostic feature for tool–x–shift
r_{inner}	Inner radius of the functional evaluation region
r_{outer}	Outer radius of the functional evaluation region
RMS	Root Mean Square of point-to-surface distances
S	Set of intersection points of neighbouring main directions (basis for r_e)
t_{nom}	Nominal tooth thickness
t_{act}	Actual tooth thickness
Δt	Tooth thickness deviation (diagnostic feature for axial infeed)
$T(k)$	Pitch deviation of tooth k
$\bar{T}$	Mean pitch deviation across all teeth
x, y, z	Cartesian coordinates in the gear coordinate system
y_i	Calculated normal deviation value at grid point i
z_i	Axial/profile coordinate of grid point i
Z	Number of teeth
α_2	Theoretical pressure angle according to Roth
α_{act}	Actual pressure angle extracted from measurement
α_n	Normal pressure angle (spur pinion)
Δx	Tool displacement in x-direction (tangential shift)
Δz	Tool displacement in z-direction (axial infeed / penetration)
Δz_i	Axial spacing between slicing planes
$\theta_{\text{align}}(k)$	Alignment rotation angle of tooth k
$\theta_{\text{ideal}}(k)$	Ideal angular tooth position of tooth k
θ_{tilt}	Tool tilt / wobble angle (spindle runout)
$\vec{v}_{\text{Flank1}}$	Direction vector of the first tooth flank
$\vec{v}_{\text{Flank2}}$	Direction vector of the second tooth flank

Symbol	Description
$\vec{v}_{\text{Main}}$	Averaged tooth main direction

4.2 Pre-processing and Registration

The evaluation is based on optical 3D scans exported as STL files, providing a full-surface representation of the manufactured flank topography. These data form the geometric basis for all subsequent processing steps.

A central aspect of the proposed workflow is its model-agnostic referencing strategy. Instead of relying on a specific software environment or data origin, the procedure only requires the nominal geometry to be provided as a discretized 3D model (STL). This ensures that the approach remains universally applicable across heterogeneous data sources. In practice, nominal geometries may originate from:

- **Profesional gear design software** (e.g., KISSsoft [12], HyGEARS [9], ESCO [5]),
- **Analytically defined reference models** based on such as Roth [22], Gindin et al. [7], Hochrein et al. [11], or Litvin [16],
- **Simulation-derived geometries** generated by virtual process models, e.g. [2].

Since the measurement data initially exist in an arbitrary spatial orientation, precise registration against the chosen nominal geometry is required.

4.2.1 Registration Strategy The registration begins with a coarse RANSAC alignment and a subsequent ICP refinement against the nominal geometry (schematically visualized in Fig. 4).

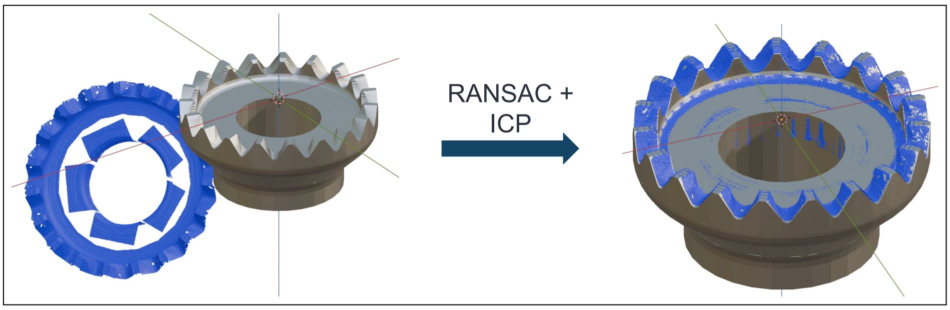

Figure 4: Coarse alignment via RANSAC followed by fine registration via ICP

While this is sufficient to obtain a stable pose, a point-cloud-based alignment alone does not ensure comparability. In optical measurements, varying point densities and measurement-focus areas can shift the centroid of the data, causing the transformation to depend on the local point distribution rather than the actual geometry. As a result, identical parts may end up in slightly different coordinate frames, which introduces non-functional deviation in the evaluation. For this reason, a second registration stage based on geometric reference elements is applied. Depending on data availability and the condition of the measured part, different features may serve as references, including inner or outer cylindrical surfaces, the planar surface at the tooth heads, or - in special cases - the tooth geometry itself. In practice, the inner cylinder has proven to be the most reliable rotational reference, as it is largely insensitive to local flank deviations. The planar surface on the tooth heads, provided it has been cleanly machined, is used as the axial zero reference of the coordinate system.

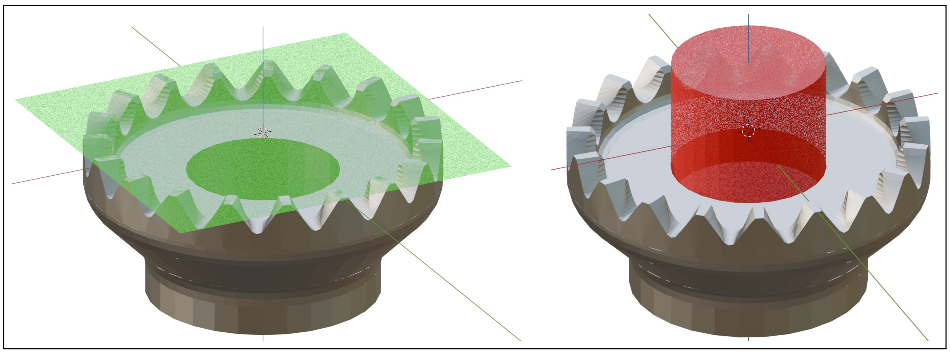

Figure 5: Geometric reference elements used for functional registration

A complementary registration strategy that aligns the part directly via the toothing will be presented in Section 4.5, offering an alternative for cases where cylindrical or planar reference surfaces are incomplete, damaged, or not sufficiently reliable for establishing the coordinate system.

4.2.2 Segmentation and Single Tooth Referencing For the evaluation of independent profile and flank line deviations, the face gear is decomposed into individual tooth segments. This is done by analyzing a cylindrical section in the region of the inner radius. Minima in the height profile of this section define the inter-tooth spaces and allow for the extraction of isolated tooth meshes (schematically visualized in Fig. 6).

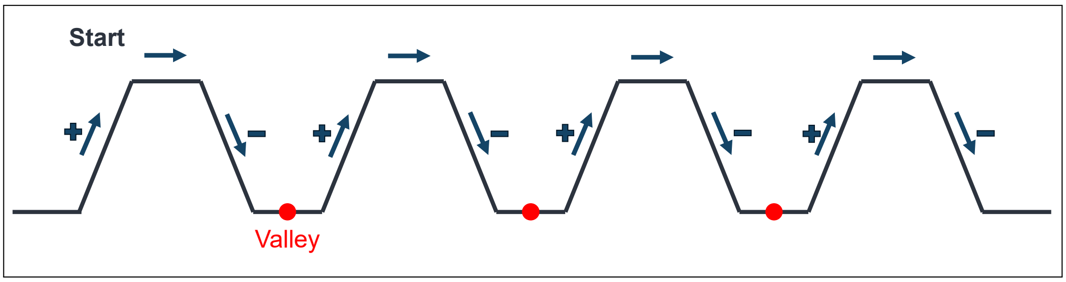

Figure 6: Segmentation of teeth via Peak-Valley detection

After segmentation, fine alignment is performed at the single-tooth level (schematically visualized in Fig. 7). This step is necessary because pitch errors would otherwise affect the evaluation of profile and flank line deviations. In addition to the circumferential correction, a radial adjustment is applied to suppress runout-induced offsets, ensuring that pitch and runout errors are not mapped into the profile or flank line alignment. The goal is an isolated analysis of the three-dimensional form deviations of individual teeth; therefore, existing pitch errors must be computationally corrected. To this end, each tooth is transformed around the rotation axis so that it best matches the ideal nominal tooth geometry.

For the evaluation of left- or right-sided pitch errors, the fine alignment can be performed exclusively on the corresponding left or right tooth flank, respectively. In this case, the opposite flank is intentionally excluded from the optimization to avoid cross-coupling effects and to ensure a flank-specific assessment.

The optimization criterion is the minimization of the Root Mean Square (RMS) of the point-to-surface distances between the actual and nominal geometry:

$$\mathrm{RMS} = \sqrt{\frac{1}{N}\sum_{i=1}^{N} d_i^2} \tag{2}$$

The rotational displacement $\theta_{\mathrm{align}}(k)$ determined here is stored and later serves as the basis for calculating the pitch deviation. This decouples the form deviation from the positional deviation of the tooth.

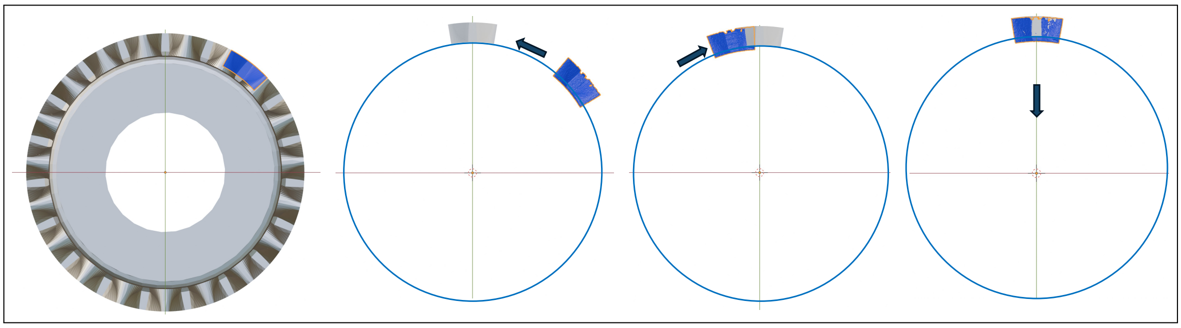

Figure 7: Single tooth alignment for minimizing point-to-surface distances

4.3 Grid-based Distance Calculation

To determine the nominal-actual deviations, an equidistant grid is first generated on the mid-tooth YZ-plane of the nominal geometry (schematically visualized in Fig. 8). This grid is defined such that it lies entirely within a rectangular functional evaluation area, ensuring that no grid points outside the effective gearing area are considered.

From each grid point, rays are cast in the positive and negative x-directions using a raycasting approach to determine the corresponding intersection points with the nominal geometry. These intersection points define the nominal points for distance calculation. Based on the associated triangular surfaces of the STL representation, local normal vectors are determined. Rays are then cast along these normals to determine the corresponding points on the previously aligned actual geometry.

The point-wise, signed normal distance between nominal and actual geometry is thus given by:

$$d_{\text{norm}} = \text{Distance}(\text{Nominal}, \text{Actual}) \tag{3}$$

Positive distances indicate material excess, while negative values correspond to a material deficit. Through this procedure, the originally unstructured actual point cloud is converted into an ordered data structure of profile and flank lines.

To restrict the evaluation area in accordance with the specific geometry of the face gear, established analytical flank models such as those proposed by [7] or [11] can be employed. These models provide an explicit geometric description of the tooth flank and allow the functional inspection region to be derived directly from the underlying gear geometry rather than being defined heuristically.

In particular, the undercut region of the face gear exhibits a complex three-dimensional progression along the flank surface, which renders a direct evaluation over the entire scanned area impractical. To avoid misinterpretations caused by geometrically non-functional regions, the functional evaluation area is therefore defined in a geometry-driven manner. Following the approach of Gindin & Bilen 2025 et al. [7], the tooth flank is parametrized using analytical expressions for the projected flank coordinates X_p and Y_p (see equations 4 and 5). Based on these equations, the functional evaluation area is conventionally represented as a rectangular region in the YZ-plane.

The position and extent of this rectangle are formulated as an optimization problem, in which the boundaries of the evaluation area are determined such that the usable functional flank region is maximized while excluding undercut and transition zones. The optimization is performed based on the analytical flank equations, and the distance grid for deviation analysis is spanned exclusively within this optimized evaluation area.

$$X_p = x \cdot \cos\bigl(\Phi(x)\bigr) - \frac{1}{u \cdot \varphi'(x)} \cdot \sin\bigl(\Phi(x)\bigr), \tag{4}$$

$$Y_p = x \cdot \sin\bigl(\Phi(x)\bigr) + \frac{1}{u \cdot \varphi'(x)} \cdot \cos\bigl(\Phi(x)\bigr), \tag{5}$$

The approach is schematically visualized in the following figure:

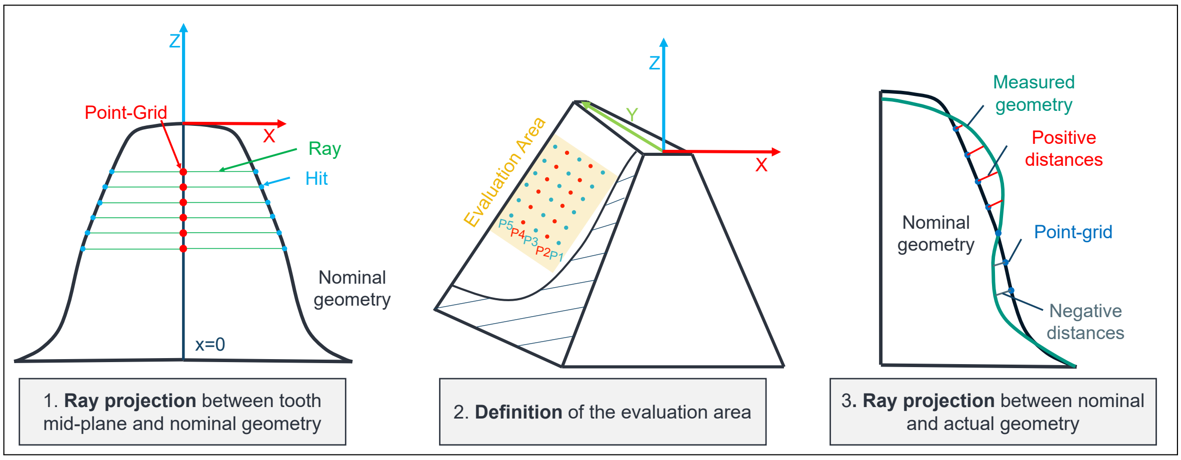

1. **Ray projection** between tooth mid-plane and nominal geometry

2. **Definition** of the evaluation area

3. **Ray projection** between nominal and actual geometry

Figure 8: Visualization of distance evaluation steps.

4.4 Derivation of Geometric Features for Quality Control

Based on the computed normal distances between nominal and actual geometry, considering only the relevant evaluation ara by following the procedure in subsection 4.3 characteristic parameters relevant for quality control are derived. In analogy to the principles defined in [26], a linear regression is applied to the evaluated point sets in order to quantify systematic deviations. From this regression, the key descriptors are obtained. They are shown in 9. Together, these quantities form a consistent feature set that enables both geometric assessment and subsequent feedback for process correction.

4.4.1 Profile and Flank Line Deviation For each measured profile and flank line, a linear regression is performed according to the procedure in [26] in order to determine the dominant deviation direction:

$$\hat{y}_i = a \cdot z_i + b, \tag{6}$$

where z_i denotes the line coordinate along the profile or flank line and y_i the corresponding measured deviation. The coefficient a represents the slope of the regression line and thus quantifies the systematic inclination of the deviation along the evaluated line, while b denotes the intercept and corresponds to a constant offset of the deviation. Based on the regression line, the characteristic deviation parameters are derived as follows. The *total deviation* F is defined as the difference between the maximum and minimum measured deviation values:

$$F_\alpha = \max(y_i) - \min(y_i). \tag{7}$$

The *slope deviation* f_H is represented by the slope a of the regression line and characterizes a systematic inclination of the profile or flank line.

The *form deviation* f_f describes the deviation from the idealized linear trend. It is computed from the residuals:

$$a_i = y_i - (a \cdot z_i + b) \tag{8}$$

as

$$f_{f\alpha} = \max(|\max(a_i)|, |\min(a_i)|). \tag{9}$$

All deviation parameters are evaluated separately for the left and right flanks and are subsequently aggregated statistically over all teeth as described in Section 4.4.4.

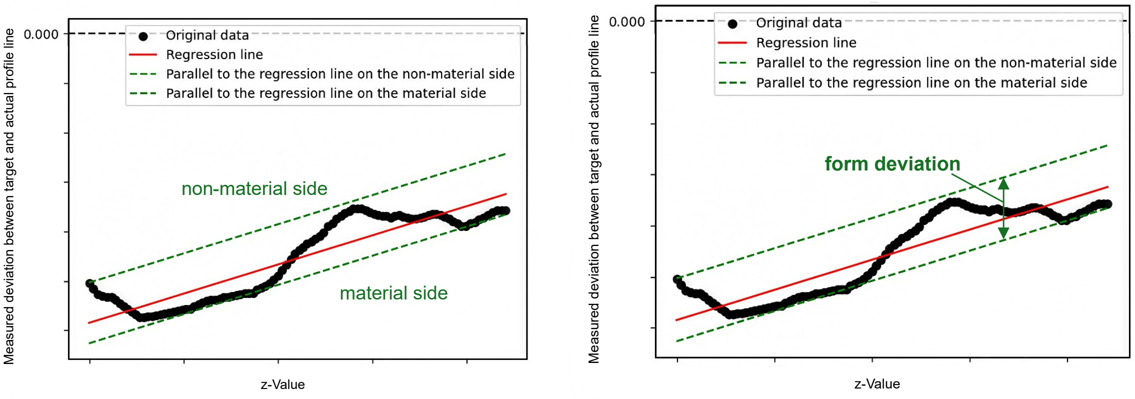

(a) Measured profile line (b) Form deviation

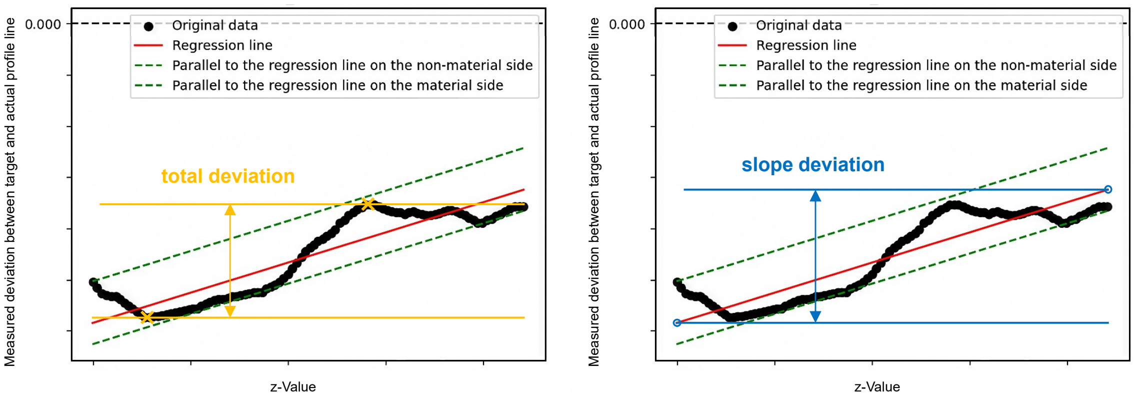

(c) Total deviation (d) Angle deviation

Figure 9: Evaluation of profile line deviations based on linear regression. The evaluation is equivalent for flank lines, z is then substituted by y

4.4.2 Pitch Deviation The pitch deviation $T(k)$ is determined from the previously stored rotation angles of the single tooth alignment. This approach prevents local flank form errors from distorting the pitch measurement, as the position of the tooth is considered as a whole.

$$T(k) = \theta_{\text{align}}(k) - \theta_{\text{ideal}}(k) \tag{10}$$

with

$$\theta_{\text{ideal}}(k) = (k-1) \cdot \frac{360^\circ}{Z} \tag{11}$$

4.4.3 Pressure Angle To verify the gear geometry, the actual pressure angle α_{act} is determined via regression analysis of the profile lines and compared with the theoretical nominal value according to Roth [22]:

$$\alpha_2 = \arccos\left(\frac{d_2}{m_n\, z_2\, \cos(\alpha_n)}\right). \tag{12}$$

The corresponding slope parameter is given by $a = \tan(\alpha_2)$. This enables a CAD-independent verification of the gear geometry.

4.4.4 Derivation of Global Metrics via Tooth-wise Averaging It must be emphasized that the described procedure is not applied to a single profile or flank line alone. For each tooth, multiple profile and flank sections are extracted along the tooth axis and evaluated individually. The resulting characteristic values (F_α, $f_{f\alpha}$, $f_{H\alpha}$, etc.) are then averaged on a per–tooth basis in order to obtain a representative metric that filters out purely local noise and allows the identification of systematic deviations. Subsequently, a second aggregation step is performed across all teeth of the gear. This global averaging highlights error mechanisms that manifest consistently throughout the component (e.g., tangential shift, wobble, feed variation), while random measurement artefacts cancel out.

4.5 Development of a Feature for Predicting Tool-x-Shift Error

Local profile metrics alone are insufficient to assess global symmetry deviations. When the hobbing tool is displaced in the x-direction, the tooth centre axes (tooth main directions) no longer converge towards a common centre but diverge outward. Instead of intersecting in a single point, they form a circular envelope around the gear origin [2]. This observation forms the basis of the feature developed here. The radius of this envelope is referred to as the **Eccentric Radius** r_e, which increases proportionally to the magnitude of the tool-x-shift Δx. Two equivalent determination routes are introduced for computing the tooth main directions before evaluating the eccentric radius:

1. **Method A: Flank-based regression of the tooth centre directions (Fig. 10a)**
2. **Method B: Substitute-tooth model via profile extrapolation (Fig. 11)**

Both procedures result in one direction vector per tooth and are therefore interchangeable with respect to the subsequent evaluation. Once the main directions are determined, the computation of r_e proceeds identically for both methods.

4.5.1 Preprocessing and Segmentation Intersecting the aligned face gear mesh with several planes parallel to the XY-plane yields flank lines at defined heights. The planes are placed at discrete z-levels

$$z_i = z_{\min} + (i-1)\,\Delta z, \qquad i = 1, \ldots, n, \tag{13}$$

so that each plane cuts the STL geometry and produces one set of section curves per tooth. Non-functional regions are removed by applying a radial window between an inner and outer reference radius, and the remaining segmented flank lines serve as the basis for evaluation.

4.5.2 Method A: Main Directions via Flank Regression A linear regression is applied to each flank. The mean of both flank direction vectors yields the tooth main direction:

$$\vec{v}_{\text{Main}} = \tfrac{1}{2}(\vec{v}_{\text{Flank1}} + \vec{v}_{\text{Flank2}}). \tag{14}$$

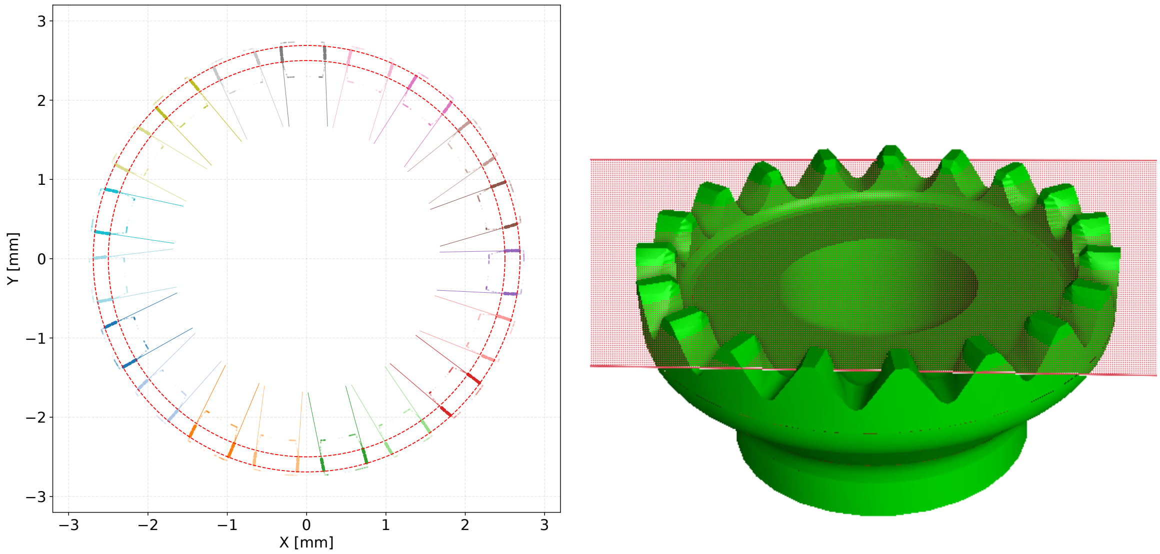

(a) Flank regressions determining the main directions.

(b) Planar intersections diverging under tool-x-shift.

Figure 10: Method A: Determination of tooth main directions from flank geometry.

4.5.3 Method B: Substitute Tooth Model via Profile Extrapolation Regression lines of the left and right profiles are extrapolated until they intersect to form an imaginary tooth tip. A regression line connecting the tips yields an equivalent main direction:

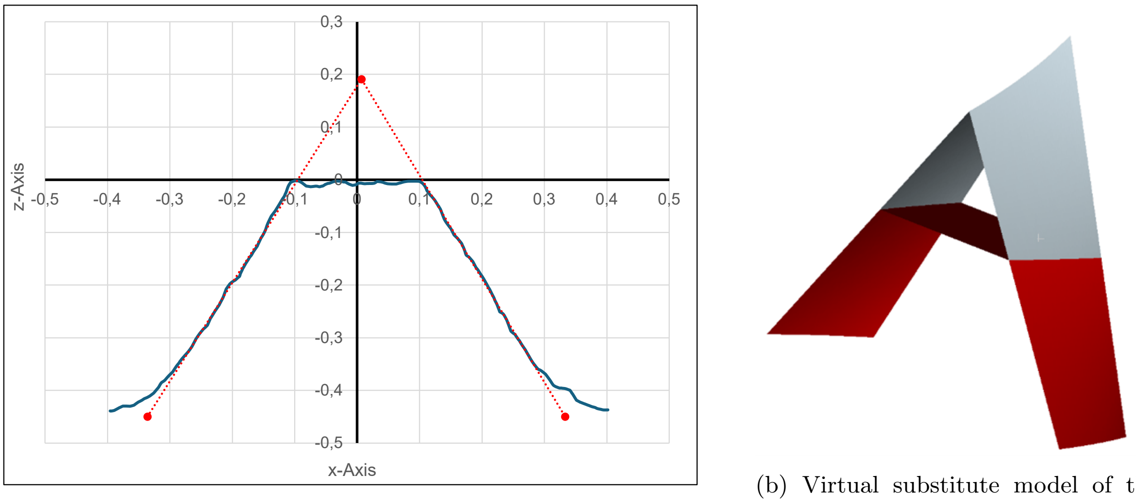

(a) Profile section with regression line, extrapolated tip and taper limit used as principal axis.

(b) Virtual substitute model of the tooth tip through profile extrapolation.

Figure 11: Method B: Profile-based substitute reference construction. (a) Regression-based determination of taper limit as principal axis, (b) extrapolated tooth tip as virtual reference.

4.5.4 Unified Evaluation of Both Methods: Computation of the Eccentric Radius Independent of whether the main directions are obtained from Method A or Method B, the evaluation procedure is identical. The main directions form a set of straight lines whose intersections define a circular envelope. The eccentric radius is defined as the *largest circle* that can be placed between these lines.

The radius is determined by an iterative optimization procedure in which the circle center is successively repositioned and the radius updated until the maximum feasible radius is reached.

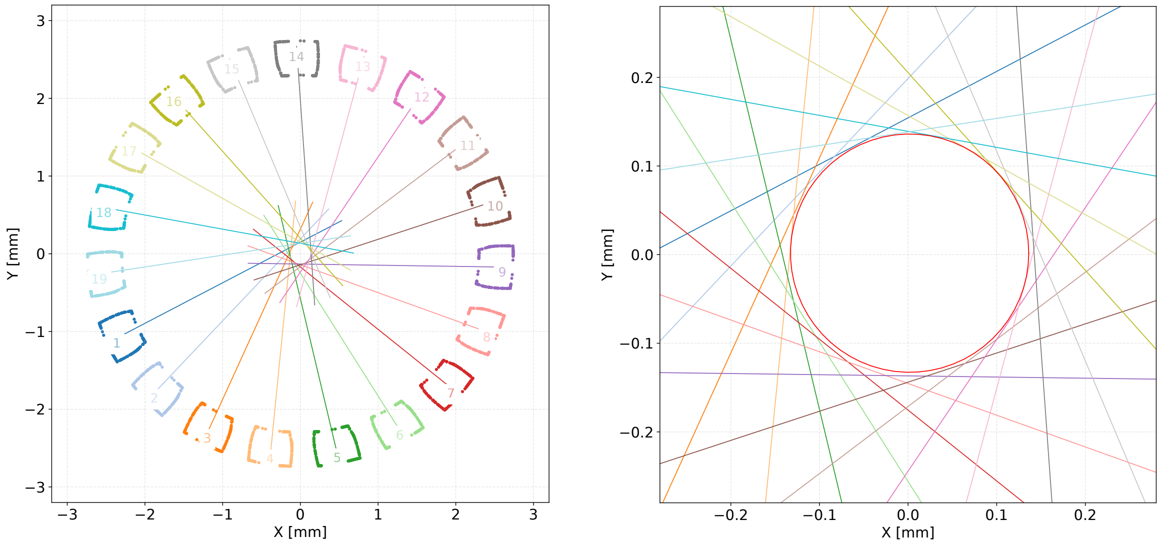

(a) Envelope formed by all main directions.

(b) Fitted circle defining the eccentric radius r_e.

Figure 12: Unified evaluation of Method A and B: determination of the eccentric radius r_e.

4.5.5 Interpretation

$$r_e \approx 0 \Rightarrow \text{no shift / correct tool alignment}, \quad r_e > 0 \Rightarrow \text{systematic tool-x-shift present.}$$

Evaluating r_e across multiple height levels additionally provides a measure for global axis alignment and tilt in the workpiece coordinate system.

4.6 Development of a Feature for Detecting Tool-z-Shift and Penetration Error

Profile- and flank-based metrics such as F_α and F_β are inherently shape-based descriptors and quantify deviations in local flank form, but remain largely insensitive to global, parallel offsets of both flanks. While such equidistant offsets do not affect the functional meshing geometry in cylindrical gears, face gears exhibit axial sensitivity: a systematic displacement of the hobbing tool in the z-direction modifies penetration depth and thus tooth thickness, which cannot be inferred from F_α or F_β alone. To overcome this limitation, a Tooth Thickness Deviation (TTD) metric is introduced to capture equidistant flank displacements that manifest as uniform translations in normal direction and, although form-invariant, alter the functional tooth thickness and encode crucial information for tool positioning and feed calibration. For each tooth, nominal thickness is computed via

$$t_{\mathrm{nom}} = x^{\mathrm{R}}_{\mathrm{nom}} - x^{\mathrm{L}}_{\mathrm{nom}}, \tag{15}$$

with (L, R) denoting left/right flanks and x aligned with the primary separation direction. Actual flank coordinates follow from nominal–actual comparison

$$x^{\mathrm{L,R}}_{\mathrm{act}} = x^{\mathrm{L,R}}_{\mathrm{nom}} + d^{\mathrm{L,R}} n^{\mathrm{L,R}}_{x}, \tag{16}$$

yielding the actual thickness

$$t_{\mathrm{act}} = x^{\mathrm{R}}_{\mathrm{act}} - x^{\mathrm{L}}_{\mathrm{act}}, \tag{17}$$

and the Tooth Thickness Deviation

$$\Delta t = t_{\mathrm{act}} - t_{\mathrm{nom}}. \tag{18}$$

Positive values indicate increased thickness, negative values reduced thickness and thus increased penetration depth. Aggregation across section heights gives

$$\Delta t_z = \frac{1}{N} \sum_{i=1}^{N} \Delta t(z_i), \tag{19}$$

and the per-tooth map

$$\{\Delta t_z\}_k, \quad k = 1, \ldots, Z, \tag{20}$$

permits computation of global statistics such as $\overline{\Delta t}$, $\Delta t_{\max}$, $\Delta t_{\min}$, and $\sigma_{\Delta t}$. The TTD feature is sensitive to tool-z-shift and penetration and complements form-based metrics (F_α, F_β) that are otherwise blind to uniform flank translations; this enables decoupling axial misalignment from shape-based deviations and improves compensation and feed calibration during face gear hobbing.

4.7 Hypothesis-Based Validation of the Evaluation Strategy

To assess whether the defined feature set is suitable for identifying process-induced deviations on face gears, three exemplary error hypotheses are formulated. While a wide range of deviation mechanisms may occur in practice, the focus is deliberately placed on these representative cases to illustrate how characteristic manufacturing deviations are reflected in the extracted features. These hypotheses form the conceptual basis for the subsequent validation and are derived from characteristic deviation mechanisms.

H1 - Axial Shift (Δz): An axial displacement of the hobbing tool alters the effective penetration depth and therefore modifies the functional tooth thickness. In contrast to involute spur gears, face gears exhibit a height-dependent pressure angle and are more sensitive to axial spacing. Consequently, Δz not only affects the tooth thickness but also propagates into the local profile and flank angles. A systematic response is therefore expected in the Tooth Thickness Deviation (TTD) and in the angular deviation metrics ($F_{h\alpha}, F_{h\beta}$), while form-related metrics remain comparatively stable and no left–right asymmetry emerges.

H2 - Tangential Shift (Δx): A tangential misalignment causes a left–right asymmetry in the functional tooth space. The displacement side gains functional contact area, while the opposite side tends toward undercut. This asymmetry is expected to be reflected in an imbalance of profile and flank deviations (e.g., F_α/F_β) and in the dedicated shift indicator defined in Section **??**.

H3 - Tool Wobble: Dynamic tilt of the tool introduces a time-dependent engagement of the cutting edges and results in characteristic facet formation on the tooth flanks. This error mechanism manifests predominantly in increased profile- and flank-form deviations ($f_{f\alpha}$ and $f_{f\beta}$), and consequently also elevates the corresponding total deviations (F_α and F_β). In contrast to static error modes, wobble is expected to trigger irregular, locally varying deviations in the surface topography.

5 Exemplary Application of the Holistic Evaluation Method

In this chapter, the holistic evaluation method is applied to a data set of **225 experimentally manufactured face gears** produced as **test geometries** for validation purposes. These components do not originate from a serial production process but were specifically designed for a controlled laboratory experiment. A statistical design of experiments was implemented in which the tangential tool shift Δx, axial infeed Δz, and wobble were systematically varied across predefined levels.

At the scale of $m = 0.25\,\text{mm}$, face gears are highly sensitive to small process deviations and exhibit pronounced geometric responses. Optical acquisition contributes additional measurement variation, which-rather than being detrimental-provides a realistic validation environment in which the hypotheses from Section 4.7 can be tested.

The central objective at this stage is not to evaluate production quality, but to assess whether the expected responses of the defined geometric features to specific induced deviations can be consistently observed in practice. The following sections analyze the measurement results and discuss the extent to which the evaluation method supports drawing interpretable, process-related conclusions.

5.1 Experimental Procedure

The experiment investigates translational tool misalignments in the x- and z-direction, as well as dynamic wobble (tilting) of the tool (schematically depicted in figure 13). These deviations represent realistic production error modes, as they tend to drift over time due to mechanical wear, thermal effects, or fixture instability in the hobbing process. The extracted quality features are subsequently used to detect these errors in the physical workpieces and to derive compensating adjustments. This represents the core objective of the proposed quality evaluation methodology. Table 2 summarizes the selected factors and factor levels of the Design of Experiments.

Table 2: Overview of factors and factor levels in the Design of Experiments

Factor	**Unit**	**Levels**
Wobble (tilt)	µm	0 | 5 | 9
Axial infeed	mm	−0.10 | − 0.05 | 0 | 0.05 | 0.10
Shift (lateral displacement)	mm	−0.10 | − 0.05 | 0 | 0.05 | 0.10

Figure 13 illustrates the implemented parameter configurations and their physical interpretation.

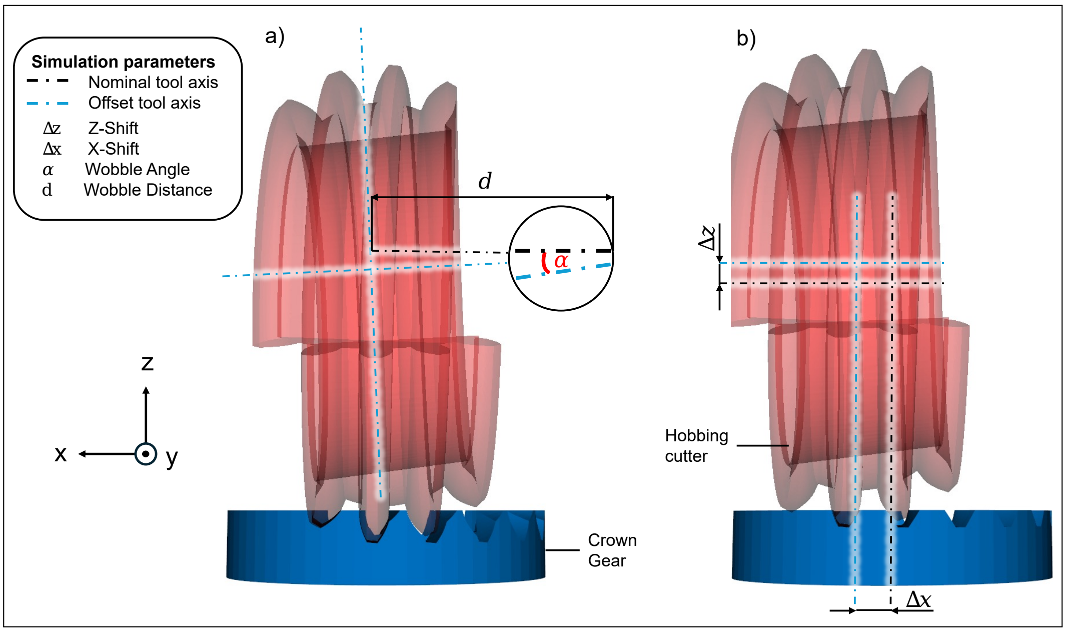

Figure 13: Visualization of the manufacturing parameters. [2]

How these deviations propagate into the resulting gear geometry is discussed in detail in [2].

5.2 *Measurement Setup*

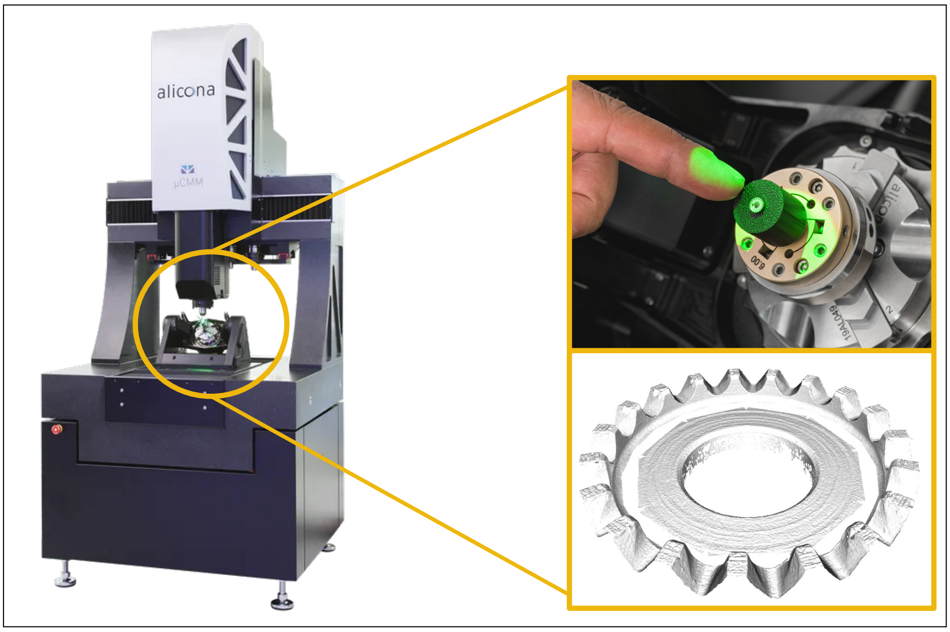

Figure 14: Left: Alicona µCMM [1]. Top right: measurement setup of the investigated face gear. Bottom right: resulting point cloud (STL) used for evaluation.

All face gears were measured using an Alicona µCMM based on focus variation. This system acquires full-field 3D point clouds, which are exported as STL meshes for subsequent evaluation. Measuring micro-scale components with a module of $m = 0.25\,\mathrm{mm}$ presents a significant metrological challenge. The angular flank geometry of face gears additionally results in surface regions that cannot be resolved from certain viewpoints, leading to local artefacts, missing data, and increased measurement uncertainty. These characteristics make the presented dataset an ideal stress test for the proposed evaluation workflow.

5.3 *Experimental Validation of the Hypotheses*

Building upon the hypothesis framework introduced in Section 4.7, the following analysis evaluates whether the defined feature set reacts in a systematic and interpretable manner when exposed to controlled manufacturing deviations. To isolate error signatures, real face gears were produced with intentionally introduced perturbations in the axial feed Δz, the tangential position Δx, and wobble. Each component was then measured and evaluated using the evaluation pipeline defined in Chapter 4.

The objective of this section is not to determine absolute manufacturing accuracy, but to assess the *diagnostic consistency* of the feature responses and to verify whether the hypothesized relationships (H1–H3) can be observed experimentally.

5.3.1 *Validation of Hypothesis H1: Sensitivity to Axial Shift*

Before validating Hypothesis H1, the extracted feature quantities are briefly exemplified for a subset of measured parts. Using the feature computation approach introduced in Section 4, the mean profile slope deviation $F_{h\alpha}$, the mean flank slope deviation $F_{h\beta}$, and the tooth thickness deviation Δt were extracted for all measured parts. These three quantities constitute the core feature set used for the validation of the axial sensitivity. The validation is performed over the full dataset rather than restricted subsets, as the influence of Δz is expected to be preserved even under interfering variation in wobble and tangential shift.

Table 3: Example of extracted feature quantities obtained from the measurement data.

Nr.	**wobble [µm]**	**Δx [mm]**	**Δz [mm]**	**$F_{h\alpha}$ [°]**	**$F_{h\beta}$ [°]**	**Δt [mm]**
155	1	0	-0.05	0.0051	-0.0015	-0.0465
161	1	0	-0.05	-0.0036	0.0038	0.0361
162	1	0	0.10	-0.0034	0.0039	0.0386
168	1	0	-0.05	-0.0030	0.0036	0.0312
171	1	0	0.05	0.0016	-0.0006	-0.0179
172	1	0	0.05	0.0052	-0.0018	-0.0558
174	1	0	0.10	-0.0047	0.0062	0.0761
176	1	0	-0.10	-0.0050	0.0062	0.0752
180	1	0	-0.10	-0.0043	0.0064	0.0766
191	1	0	0.00	0.0008	0.0001	-0.0119
195	1	0	0.00	0.0007	0.0001	-0.0132
202	1	0	0.05	0.0046	-0.0022	-0.0569
206	1	0	0.10	0.0050	-0.0027	-0.0678
210	1	0	-0.10	-0.0055	0.0066	0.0780
214	1	0	0.00	-0.0020	0.0028	0.0283

Feature response over axial shift. For Hypothesis H1, the axial tool displacement Δz is compared against the three extracted feature quantities. Figures 15, 16 and 17 show the corresponding C-diagrams. All three features exhibit clear and monotonic relations to Δz, despite visible scatter arising from measurement uncertainties, segmentation inaccuracies and occasional incomplete surface reconstruction. In particular, the feature distributions for the groups with axial shifts of 0.05 mm and 0.10 mm appear highly similar in Figures 15–17. This effect is attributed to the increased tool penetration from $\Delta z \geq 0.05$ mm, which locally removes the tooth head used for the point cloud alignment. As a consequence, the registration is performed only on the remaining tooth tips, causing the effective height difference between the two groups to diminish in the resulting feature space.

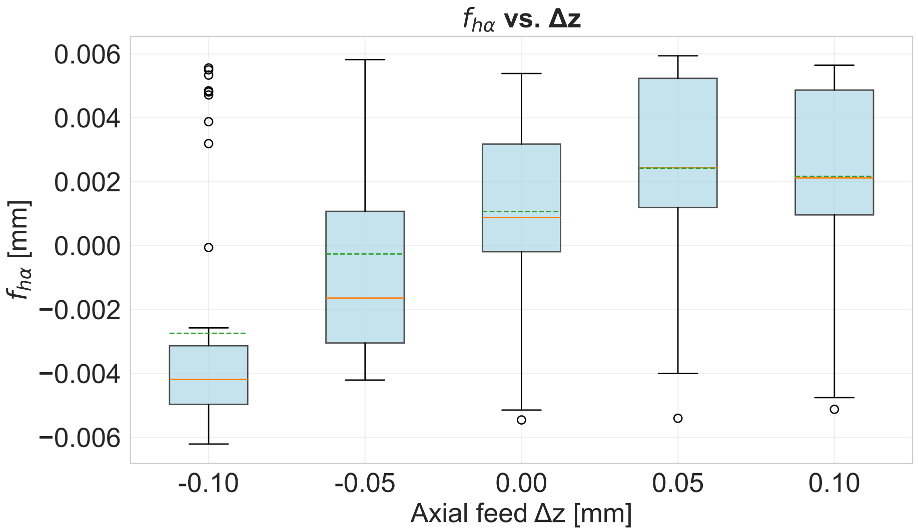

Figure 15: Profile slope deviation $F_{h\alpha}$ over axial shift Δz.

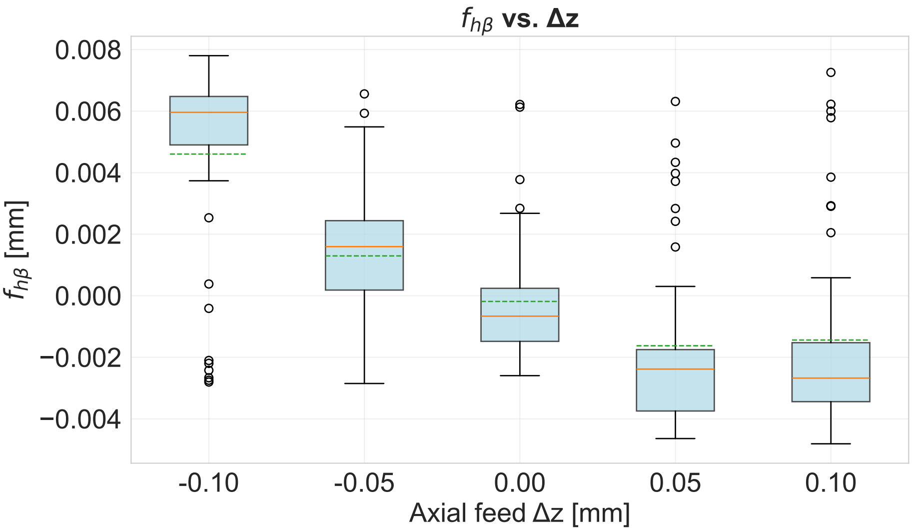

Figure 16: Flank slope deviation $F_{h\beta}$ over axial shift Δz.

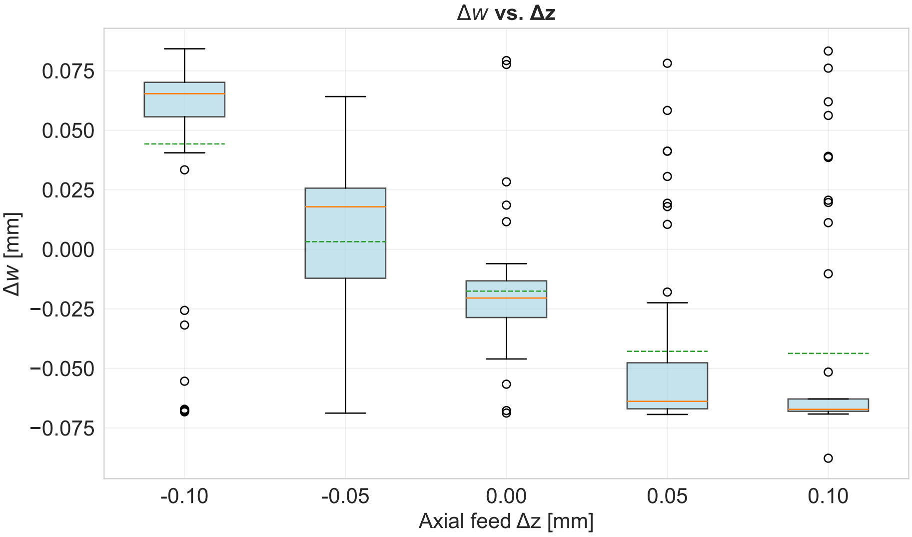

Figure 17: Tooth thickness deviation Δt over axial shift Δz.

Conclusion. The results confirm the expected axial sensitivity. All three feature quantities react in a geometrically interpretable manner to Δz, following the mechanisms discussed in Section 4.7. The monotonic relations remain visible over the full dataset, despite interfering process variation through wobble and tangential shift Δx. The observed scatter is attributable to measurement noise rather than to a weakening of the underlying functional relation. Hypothesis H1 is therefore confirmed.

5.3.2 Validation of Hypothesis H2: Sensitivity to Tangential Shift Hypothesis H2 states that a tangential tool shift Δx does not modify the effective tooth height, but laterally displaces the functional engagement zone within the tooth space. As a result, the displacement side gains load-bearing flank contact, while the opposite side loses engagement and tends towards local undercut. This geometric imbalance is expected to manifest as a characteristic left-right asymmetry in both profile and flank line deviations.

In contrast to the height-driven behavior observed for axial shifts Δz, a tangential shift is not expected to introduce a global offset in F_α or F_β. Instead, a directional split between the load-bearing and relief sides of the tooth space is assumed. The polarity and magnitude of this asymmetry should scale with the sign and amplitude of Δx and can be quantified using the shift indicator defined in Section 4.5.

To isolate the influence of Δx, the tangential shift was intentionally varied while all other setup parameters were kept nominal. The resulting left–right profile deviations and the corresponding eccentricity indicators are summarized in Table 4.

Table 4: Measured left-right imbalance in F_α and eccentricity radius r_e for tangential shift variation (Validation of Hypothesis H2).

Nr.	**wobble**	Δx **[mm]**	Δz **[mm]**	$F_{\alpha,\mathrm{L}}$ **[mm]**	$F_{\alpha,\mathrm{R}}$ **[mm]**	r_e **[mm]**
166	1	-0.05	0	-0.0059	-0.0441	-0.07954
170	1	0.10	0	-0.0063	-0.0573	0.05954
177	1	-0.10	0	0.0606	0.0401	-0.04984
181	1	0.05	0	0.0507	0.0395	-0.04684
191	1	0.00	0	-0.0195	-0.0029	-0.03319
192	1	-0.10	0	-0.0187	-0.0064	-0.13468
194	1	-0.10	0	-0.0223	-0.0072	-0.14791
195	1	0.00	0	-0.0074	-0.0043	-0.05686
196	1	0.10	0	-0.0100	-0.0044	0.09683
207	1	0.10	0	-0.0057	-0.0043	0.08744
214	1	0.00	0	0.0113	0.0221	-0.01224
217	1	0.05	0	-0.0160	-0.0036	0.02558
218	1	-0.05	0	-0.0077	-0.0004	-0.07648
220	1	-0.05	0	-0.0261	-0.0026	-0.08305
225	1	0.05	0	-0.0159	-0.0039	0.02327

Across the dataset, a consistent left-right asymmetry in both $f_{f\alpha}$ and $f_{f\beta}$ is observed as a function of Δx (see Fig. 18). The polarity of this asymmetry agrees with the sign of the imposed displacement, confirming the geometric mechanism predicted by H2. However, the magnitude of the asymmetry does not increase monotonically with $|\Delta x|$, and the pronounced scatter suggests that isolated components $f_{f\alpha,\mathrm{L/R}}$ and $f_{f\beta,\mathrm{L/R}}$ are insufficiently robust as standalone estimators for shift determination.

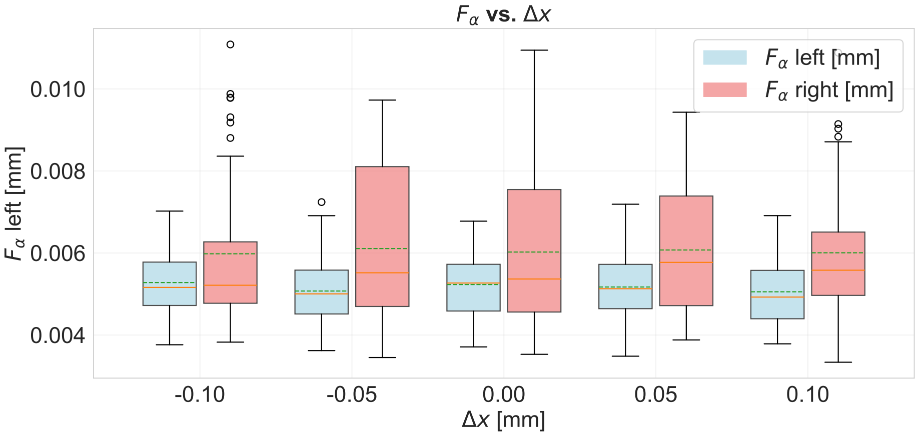

(a) Profile form deviation f_α for left and right flanks as a function of Δx.

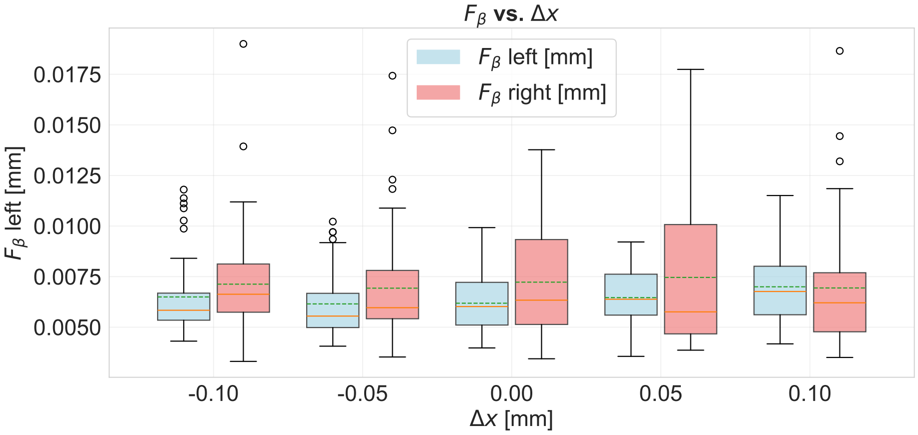

(b) Flank form deviation f_β for left and right flanks as a function of Δx.

Figure 18: Left–right comparison of form deviations as a function of Δx.

In contrast, the eccentricity indicator r_e exhibits a clear and monotonic correlation with the applied tangential shift (Table 4, Fig. 19). Both the sign and magnitude of r_e consistently reflect the imposed misalignment, including a polarity reversal at the transition point.

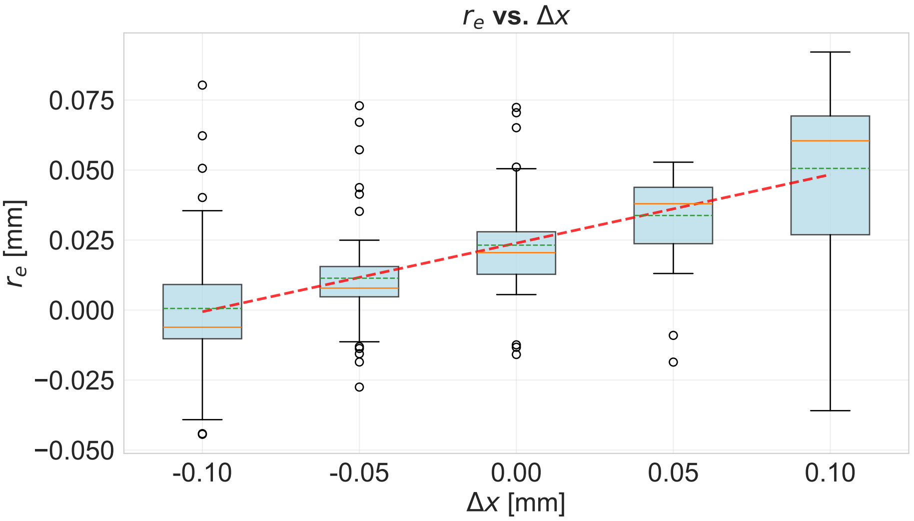

Figure 19: Eccentricity radius r_e as a function of the applied Δx.

A systematic positive bias is observed: the regression of r_e versus Δx is located predominantly above zero. This bias does not originate from measurement noise, but from the geometric mapping itself. A tangential shift Δx acts on a curved face-gear flank and induces a second-order deformation of the local flank normals. Under a linear approximation, this second-order component appears as a constant positive offset in the r_e–Δx regression.

To compensate for this bias, an empirical correction term was calibrated from the deviation behavior of the investigated dataset. The absolute deviation between the estimated and the applied tangential shifts was approximated by a linear regression (Fig. 20a), confirming that larger $|\Delta x|$ lead to increased linearization errors. The resulting empirical correction term is given by:

$$\text{Correction Term} = 0.7552 \cdot r_e - 0.0239. \tag{21}$$

For generality, the correction can be expressed in parametric form by separating a systematic tangential offset $x_{\text{calibration}}$ from the sensitivity, which is scaled with the normal module m:

$$\text{Correction Term} = 3m \cdot r_e - x_{\text{calibration}}. \tag{22}$$

The corrected shift estimate is then obtained as:

$$x_{\text{corr}} = r_e + \text{Correction Term}. \tag{23}$$

Applying this correction significantly reduces the mean relative deviation across the dataset, particularly for negative shift values. Several extreme outliers become more pronounced after correction; these can be attributed to incomplete measurement data or incorrect sign assignments.

For visualization purposes only, an additional scaling was applied in Fig. 20b to enhance the dynamic range of the corrected residuals:

$$x_{\text{corr,vis}} = r_e + 4 \cdot \text{Correction Term}. \tag{24}$$

This visualization scaling does not affect the correction model or its quantitative interpretation.

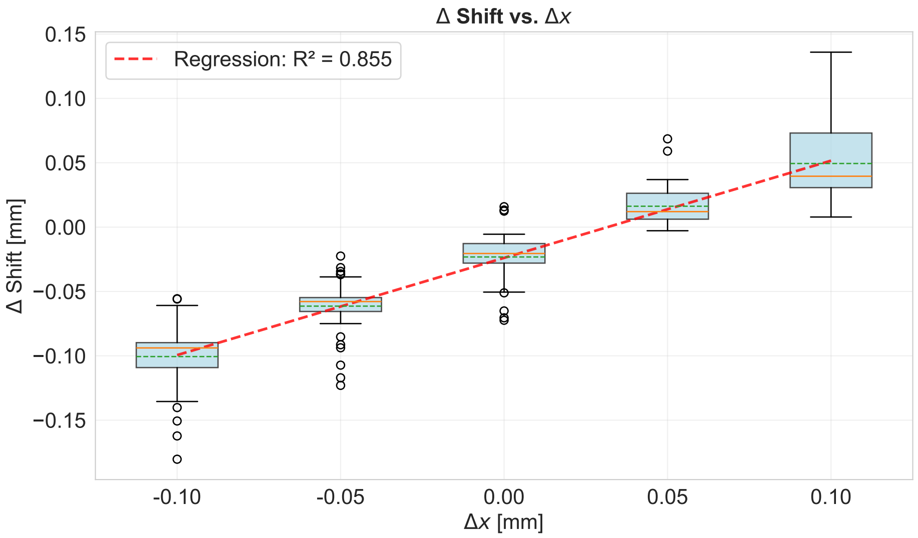

(a) Absolute deviation between r_e and the applied tangential shift Δx before correction.

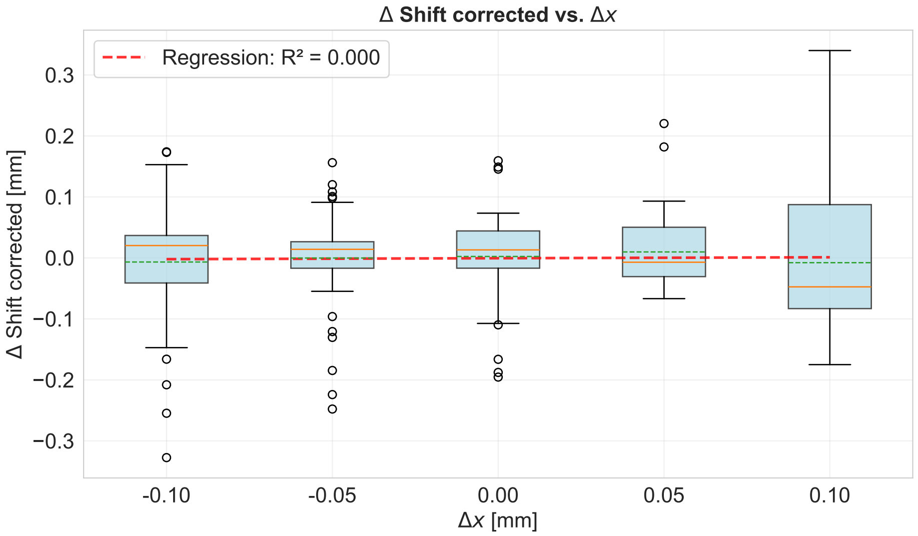

(b) Absolute deviation between r_e and Δx after correction (scaled visualization).

Figure 20: Comparison of absolute deviations before and after applying the correction term.

Conclusion. A directional left–right imbalance in F_α is observable and confirms the geometric effect predicted by H2. Due to measurement scatter, $F_{\alpha,\mathrm{L/R}}$ alone is not sufficiently robust for shift estimation. The eccentricity indicator r_e provides a polarity-stable and monotonic response and is therefore better suited for diagnosis and compensation of tangential misalignment.

5.3.3 Validation of Hypothesis H3: Sensitivity to wobble (Spindle Runout) Hypothesis H3 states that spindle wobble (runout) introduces a periodic angular disturbance into the generated tooth surfaces, resulting in alternating deviations along the circumference. In contrast to tangential or axial shift, wobble does not act as a directional displacement but as a harmonic excitation, which modulates the tooth geometry in a periodic manner. The effect is therefore not expected to manifest primarily in global offsets, but in an increase of tooth-to-tooth variation and harmonic distortion of the flank and profile form. Accordingly, wobble should be reflected predominantly in the form deviation parameters $f_{f\alpha}$ and $f_{f\beta}$.

To validate this assumption, all test parts were evaluated statistically. For each workpiece, the profile form deviation $f_{f\alpha}$ and the flank form deviation $f_{f\beta}$ were plotted against the respective wobble level (see 21)to determine whether the magnitude of form distortion correlates with the degree of spindle runout.

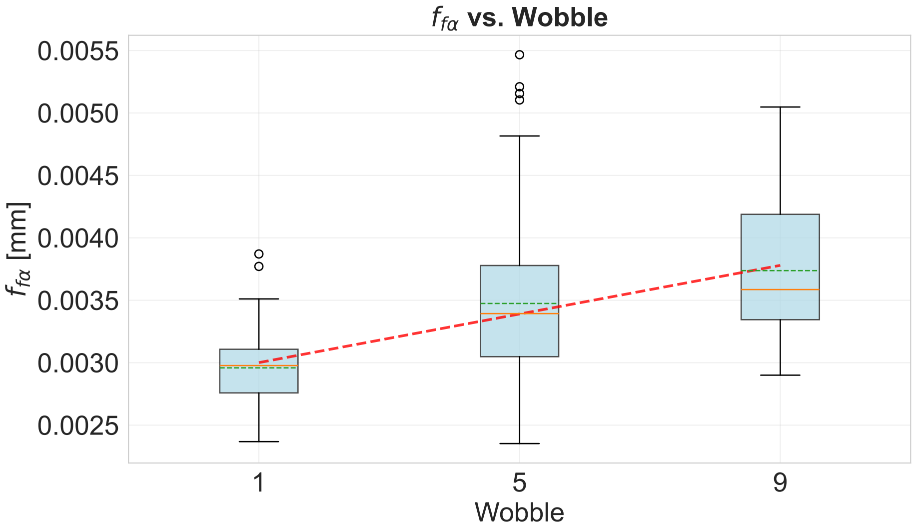

(a) Profile form deviation $f_{f\alpha}$ as a function of wobble

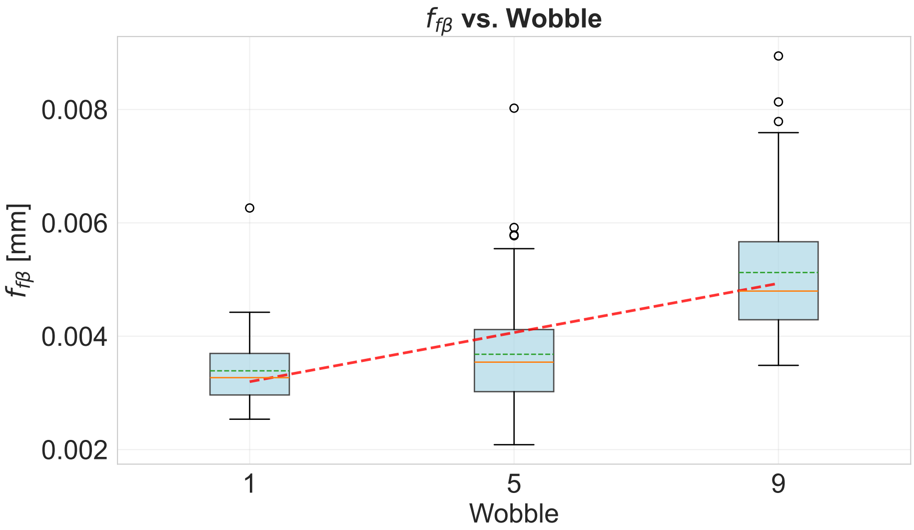

(b) Flank form deviation $f_{f\beta}$ as a function of wobble

Figure 21: Form deviation response to spindle wobble (Validation of H3)

The diagrams show that both $f_{f\alpha}$ and $f_{f\beta}$ increase with rising wobble amplitude, confirming the expected sensitivity to periodic spindle runout. While the flank form deviation $f_{f\beta}$ exhibits a clearly distinguishable separation between wobble levels, the difference in the mean profile form deviation $f_{f\alpha}$ remains comparatively small (typically on the order of 1–5 μm). This reduced effect size can be plausibly attributed to a lower effective wobble acting at the cutting engagement than nominally introduced, resulting in overlapping deviation ranges. The observed proximity of the $f_{f\alpha}$ mean values therefore does not contradict the hypothesis, but indicates a lower sensitivity of the profile direction to small harmonic excitation amplitudes.

Despite this reduced separation in $f_{f\alpha}$, the statistical trend across all investigated parts remains consistent: increasing wobble amplitude is associated with a measurable rise in form deviation, and the periodic disturbance mechanism predicted in H3 is observable in practice.

Conclusion. A statistically traceable relationship between wobble amplitude and the increase of $f_{f\alpha}$ and $f_{f\beta}$ is confirmed across the full test set. Although the mean deviation in $f_{f\alpha}$ remains within a narrow band of approximately 1–5 μm, this can be explained by a lower effective wobble input than nominally set. Overall, the results support Hypothesis H3 and validate spindle runout as a distinct, diagnostically separable error dimension within the proposed feature set.

5.4 Discussion

The experimental validation shows that the proposed feature set enables the diagnostic separation of axial infeed, tangential shift, and spindle wobble on micro face gears. Cylindrical gear inspection logic, when extended towards face gear geometry, provides sufficient observability for detecting and attributing process deviations.

However, the results also reveal practical limitations arising from optical micro-scale metrology. In particular, segmentation errors, incomplete surface reconstruction and registration artefacts introduce scatter in the extracted metrics. For larger axial infeeds, the effective alignment region is reduced due to material removal at the tooth head, which affects slope-based parameters. Despite these effects, monotonic relations with Δz remain visible, suggesting robustness against real-measurement perturbations.

For tangential shift, the left–right asymmetry behaves directionally consistent but not strictly monotonic in magnitude. In contrast, the eccentricity indicator r_e provides a clearer and polarity-stable response after bias compensation, making it a suitable estimator for tool misalignment.

Spindle wobble predominantly increases form deviations $f_{f\alpha}$ and $f_{f\beta}$, confirming the assumed harmonic disturbance mechanism; the limited sensitivity of $f_{f\alpha}$ indicates reduced effective wobble at the cutting engagement.

Overall, the experiments suggest that meaningful diagnostic information can be extracted even under non-ideal metrology conditions. Future work should investigate estimator sensitivity under additional deviation modes (e.g. cutter wear, fixture compliance) and integrate the feature set into predictive quality control and virtual metrology workflows.

6 Summary & Outlook

This work presented a feature-based evaluation strategy for micro face gears that extends classical VDI 2612 inspection logic to non-involute face gear flank geometry. The strategy combines profile-, flank- and pitch-inspired descriptors with two diagnostic features for axial infeed (tooth thickness deviation) and tangential misalignment (eccentricity radius). Together, these features establish an interpretable interface between optical and also tactile metrology and process parameters in micro-scale hobbing.

The experimental validation on 225 manufactured face gears confirms that axial infeed, tangential shift and spindle wobble can be separated based on their characteristic geometric responses. Axial deviations manifest in thickness and slope parameters, tangential misalignment is captured by the eccentricity indicator, and wobble increases form deviations. The observed relations persist despite scatter induced by optical measurement uncertainty and segmentation artefacts, indicating robustness for practical use.

The results suggest that face gear geometry provides sufficient observability for diagnostic feedback and supports the integration of feature-based inspection into process control, virtual metrology and tool correction workflows. Future work will focus on sensitivity studies for additional deviation modes (e.g. cutter wear, fixture compliance), calibration strategies for industrial deployment, and closed-loop quality regulation.

Acknowledgments

The authors would like to sincerely thank Robert Schmitt, Jochen Wacker, and Christoph Rettig from Dentsply Sirona for their valuable support of this work and for contributing their professional expertise throughout the course of the research. Furthermore, the authors gratefully acknowledge Edouard Gindin and Philip Jukl from Frenco GmbH for their support and for sharing their expert knowledge, which significantly contributed to this study.

Data availability

The underlying component data supporting the findings of this study are confidential due to industrial cooperation agreements and therefore cannot be made publicly available.

References

[1] Bruker Alicona. *Optische Koordinatenmessmaschine für komplexe Geometrien*. Jan. 2021. URL: `https://www.alicona.com/de/produkte/cmm/`.

[2] Ali Bilen et al. "A Simulation-Based Error Analysis Approach for the Crown Gear Hobbing Process". In: (2025). Under Review.

[3] Ali Bilen et al. "Harmonizing micro crown gear and spur gear geometries: A novel approach for geometry evaluation through analogous transformation". In: *Measurement: Sensors* 38 (2025). DOI: `https://doi.org/10.1016/j.measen.2025.101882`. URL: `https://www.sciencedirect.com/science/article/pii/S2665917425000765`.

[4] Dai Bing et al. “Numerical Simulation Investigation on the Windage Power Loss of a High-Speed Face Gear Drive”. In: *Energies* 12.11 (Jan. 2019). Publisher: MDPI, p. 2093. DOI: `10.3390/en12112093`.

[5] esco GmbH engineering solutions consulting. *PTM 3-6-4-0, Build 23971: Precision-Tool Manufacturing*. Published: Technical product documentation. 2020.

[6] D. Gauder et al. “Inline qualification of focus variation metrology for a series production of micro gears”. In: *tm-Technisches Messen* 89 (Jan. 2022). Number Of Volumes: 9, pp. 594–611. DOI: `10.1515/teme-2022-0047`.

[7] Edouard Gindin, Ali Bilen, and Gisela Lanza. “Eine mathematische beschreibung der flankengeometrie geradverzahnter Kronenräder”. In: *tm - Technisches Messen* (2025). Publisher: De Gruyter. ISSN: 0171-8096, 2196-7113. DOI: `10.1515/teme-2025-0033`.

[8] WENZEL Präzision GmbH. “Poster Verzahnungsparameter”. In: (Jan. 2024). Num Pages: 1. URL: `https://www.metromec.ch/images/pdf/WENZEL_Poster_Verzahnungsparameter.pdf`.

[9] Claude Gosselin. *HyGEARS Updates: Build 500.00 (04 October 2021) and Build 500.10 (09 January 2023)*. Quebec, Canada: Involute Simulation Softwares Inc., 2021. URL: `https://www.hygears.com`.

[10] F. Härtig, K. Kniel, and K. Rost. *Messung von Mikroverzahnung. Studie zum Bedarf und den Möglichkeiten der Messung von kleinen Verzahnungen*. Tech. rep. 5671. FVA-Forschungsvorhaben, 2009.

[11] Jonas-Frederick Hochrein et al. “Direct flank geometry calculation for face gears”. In: *Forschung im Ingenieurwesen* 86.3 (Jan. 2022), pp. 617–625.

[12] KISSsoftAG. *Kronenräder: Geometrie und Festigkeit - KISSsoft AG*. Ed. by yumpu.com. Jan. 2012.

[13] Fritz Klocke and Christian Brecher. *Zahnrad- und Getriebetechnik: Auslegung – Herstellung – Untersuchung – Simulation*. Hanser eLibrary. München: Carl Hanser Verlag, Jan. 2017. ISBN: 978-3-446-43140-9. DOI: `10.3139/9783446431409`. URL: `http://www.hanser-elibrary.com/doi/book/10.3139/9783446431409`.

[14] Gisela Lanza et al. “In-Line Measurement Technology and Quality Control”. In: *Metrology*. Ed. by Wei Gao. Singapore: Springer Singapore, Jan. 2019, p. 399433. ISBN: 978-981-10-4938-5. URL: `10.1007/978-981-10-4938-5_14`.

[15] Chao Lin et al. “Pitch deviation measurement and analysis of curve-face gear pair”. In: *Measurement* 81 (Jan. 2016), pp. 95–101. ISSN: 0263-2241.

[16] F. L. Litvin and A. Fuentes. *Gear Geometry and Applied Theory*. 2nd. New York: Cambridge University Press, Jan. 2011.

[17] F. L. Litvin et al. “Design and Geometry of Face-Gear Drives”. en. In: *Journal of Mechanical Design* 114.4 (Dec. 1992), pp. 642–647. ISSN: 1050-0472, 1528-9001. DOI: `10.1115/1.2917055`. URL: `https://asmedigitalcollection.asme.org/mechanicaldesign/article/114/4/642/454144/Design-and-Geometry-of-FaceGear-Drives` (visited on 03/21/2025).

[18] Faydor L. Litvin et al. *Handbook on face gear drives with a spur involute pinion*. Tech. rep. Jan. 2000.

[19] Shan Liu et al. *3D Point cloud analysis*. Springer, 2021.

[20] Xinxin Lu et al. “A measurement solution of face gears with 3d optical scanning”. In: *Materials* 15.17 (Jan. 2022). Publisher: MDPI, p. 6069.

[21] Xinxin Lu et al. “A novel mathematical model for the accurate measurement of face gears by considering the geometric deviations of multiple teeth”. In: *Measurement* 231 (Jan. 2024), p. 114545. ISSN: 0263-2241.

[22] Karlheinz Roth. *Zahnradtechnik Evolventen-Sonderverzahnungen zur Getriebeverbesserung: Evoloid-, Komplement-, Keilschräg-, Konische-, Konus-, Kronenrad-, Torus-, Wälzkolbenverzahnungen, Zahnrad-Erzeugungsverfahren*. Vol. 3. Springer-Verlag, Jan. 2013.

[23] Robert Schmitt and Edgar Dietrich. *Handbuch Messtechnik in der industriellen Produktion: Valide Messergebnisse planen, erhalten, auswerten und verteilen*. Carl Hanser Verlag GmbH Co KG, Jan. 2023. ISBN: 978-3-446-46559-6.

[24] Jinyang Tao et al. “An efficient and accurate measurement method of tooth flank variations for face gears”. In: *Measurement* 221 (Jan. 2023), p. 113486. ISSN: 0263-2241.

[25] VDI 2731 Blatt 1. *VDI 2731 Blatt 1:2009-04 – Mikrogetriebe– Grundlagen*. Tech. rep. Düsseldorf: Verein Deutscher Ingenieure (VDI), 2009. URL: `https://www.vdi.de/richtlinien/details/vdi-2731-blatt-1-mikrogetriebe-grundlagen`.

[26] VDI/VDE 2612 Blatt 1. *VDI/VDE 2612 Blatt 1:2018-11 Messen und Prüfen von Verzahnungen – Auswertung von Profil- und Flankenlinienmessungen an Zylinderrädern mit Evolventenprofil*. Dec. 2024.

[27] Shenghui Wang et al. "Digital tooth contact analysis of face gear drives with an accurate measurement model of face gear tooth surface inspected by CMMs". In: *Mechanism and Machine Theory* 167 (Jan. 2022), p. 104498.

[28] H. Andreas Zschippang, Sascha Weikert, and Konrad Wegener. "Face-gear drive: Simulation of shaping as manufacturing process of face-gears". In: *Mechanism and Machine Theory* 172 (Jan. 2022), p. 104791.